6 Supplementary Information

6.1 Construction of circular conical sections

In the main text, we describe how we divide the flat annulus into two regions – an inner region composed of isosceles triangles, and an outer region composed of arc sectors. The main text describes how the inner triangles can isometrically deform under an inner displacement (or contraction) of length Δ by tilting about the normal to the inner boundary – this gives an inner 'buckled' solution. Here, we describe how to construct the outer solution whereby the arc sectors isometrically bend into sections of right-circular cones. In other words, each arc bends into a circular profile.
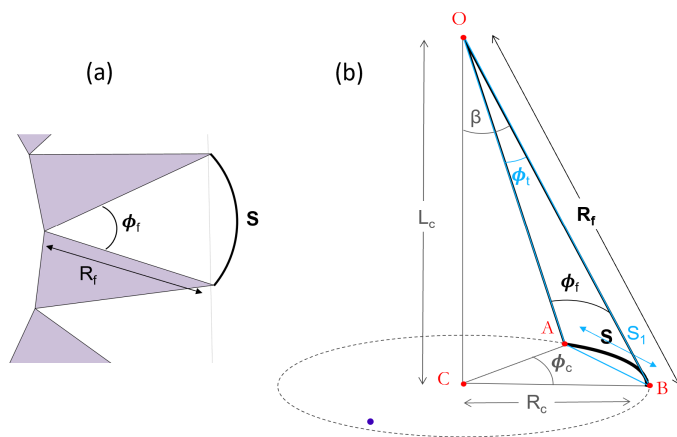

Fig. 6 Isometrically constructing a sector of a cone from a flat arc sector. (a) The flat configuration. (b) The curved configuration; the actual conical sector and its variables are depicted in black, the triangle △AOB formed by the edges of the two adjacent tilted triangles, along with its variables, is in blue, and the putative cone with its variables is in grey.

The requisite variables for our geometric construction are described in Fig. 6. In the flat state, each arc sector, lying between two adjacent flat triangles, subtends an angle ϕ_f at the common vertex of these two triangles. If the edges of the triangles have length R_f, then the length of the largest arc is $S = R_f \phi_f$. On tilting, the edges of these same triangles approach each other, so that they subtend a reduced angle ϕ_t (see SI Fig. 7a). This reduction in angle ($\Delta \phi = \phi_t - \phi_f \le 0$) constitutes the effective compressive strain $\varepsilon_{\text{cone}} = \Delta \phi / \phi_f$ for the arc sector. SI Fig. 7a shows the evolution of $\varepsilon_{\text{cone}}$ with boundary contraction Δ. We see clearly that narrower sheets feel a greater $\varepsilon_{\text{cone}}$ for the same Δ.

The excess material can be accommodated by bending the sector into a cone. The exact shape of this cone can be determined by solving the *Elastica* equation with the appropriate boundary conditions. However, for simplicity, in this paper we choose to approximate the exact shape by a circular cone. The aim then is to find the circular cone that fits in between the two adjacent triangles while exactly accommodating the excess angle $\Delta \phi$. Fig. 6b shows all the variables needed for this operation. The isometrically bent conical section has to fit inside the triangle △AOB (drawn in teal) defined by the apex 0 and the tilted edges OA and OB (see also Fig. 3 in main text). The conical section itself

is drawn in bold black. Let the circular cone have angular extent ϕ_c, and let its maximum radius be ρ_c, centred at point C. Then the conical shape can be determined from the following set of geometric constraints.

The first constraint is that of inextensibility, i.e. length conservation. This gives us:

$$S = \rho_c \phi_c = R_f \phi_f. \tag{8}$$

The second constraint involves specifying the end-to-end distance S_1 between points A and B. Thus, using the blue triangle △AOB and the grey triangle △ACB in Fig. 6b, we have:

$$S_1 = 2\rho_c \sin(\phi_c/2) = 2R_f \sin(\phi_t/2). \tag{9}$$

Eqns. (8) and (9) constitute a set of simultaneous equations for the cone variables ρ_c and ϕ_c, since R_f and ϕ_f are fixed by the flat geometry, while ϕ_t is set by the tilt of the neighbouring angles. Finally, using basic trigonometry, we have for the cone's apex angle:

$$\sin \beta = \rho_c / R_f. \tag{10}$$

In sum, we have three independent equations for three unknowns: ϕ_c, ρ_c and β (all positive-definite), which fully specify the cone in space (including the centre C). SI Fig. 7b shows a representative solution of such a constructed cone. SI Fig. 7c shows the evolution of this construction with increasing Δ.

6.2 Correcting for scalloped arc sectors

The flat arc sectors as defined above – circular arcs with their origin at the inner boundary – lead to the creation of a flat shape that is in fact a *scalloped* annulus, whose outer circumference $2mR_f\phi_f$ is greater than the expected $2\pi(1+w)$.

We can correct for this length discrepancy when constructing the bent cones, by changing $R_f \to \chi R_f$ in Eq. (8) where $\chi = \frac{\pi(1+w)}{mR_f\phi_f} \le 1$. Eq. (9) remains unchanged since it specifies the end-to-end-distance, which is set by the neighbouring tilted triangles. We note that this factor χ is smallest for samples with small w and m (wide splay η), and becomes ≈ 1 for large w and m (narrow splay).

6.3 Calculating the conical strain $\varepsilon_{\text{cone}}(\Delta)$

The inset of Fig. 7a shows the evolution of the conical strain $\varepsilon_{\text{cone}}$ with contraction Δ for our cone-triangle construction. The observations (plotted with dots) show that $\varepsilon_{\text{cone}}(\Delta)$ is linear, with the slope depending significantly on the width w of the sheet, but independent of the wavenumber m. To understand this behaviour, we analytically derive an expression for $\varepsilon_{\text{cone}}(\Delta) = (\phi_t - \phi_f)/\phi_f$.

Since ϕ_f is fixed by the initial configuration, to find $\varepsilon_{\text{cone}}$, we only need to calculate $\phi_t(\Delta)$. The angle $\phi_t(\Delta)$ can be calculated given any one of the inner triangles, the flat arc angle ϕ_f, and the tilt angle α. We use the triangle △OPQ from Fig. 7a, located in the $x - y$ plane. The annular width w gives the height of the triangle, while h gives its base. Now, instead of rotating about O, we choose to rotate the triangle about its mid-line. For this, we let X be the mid-point of OP, and we set it to be the origin $(0,0)$, as shown in Fig. 8. In similar fashion, we define Z to be the
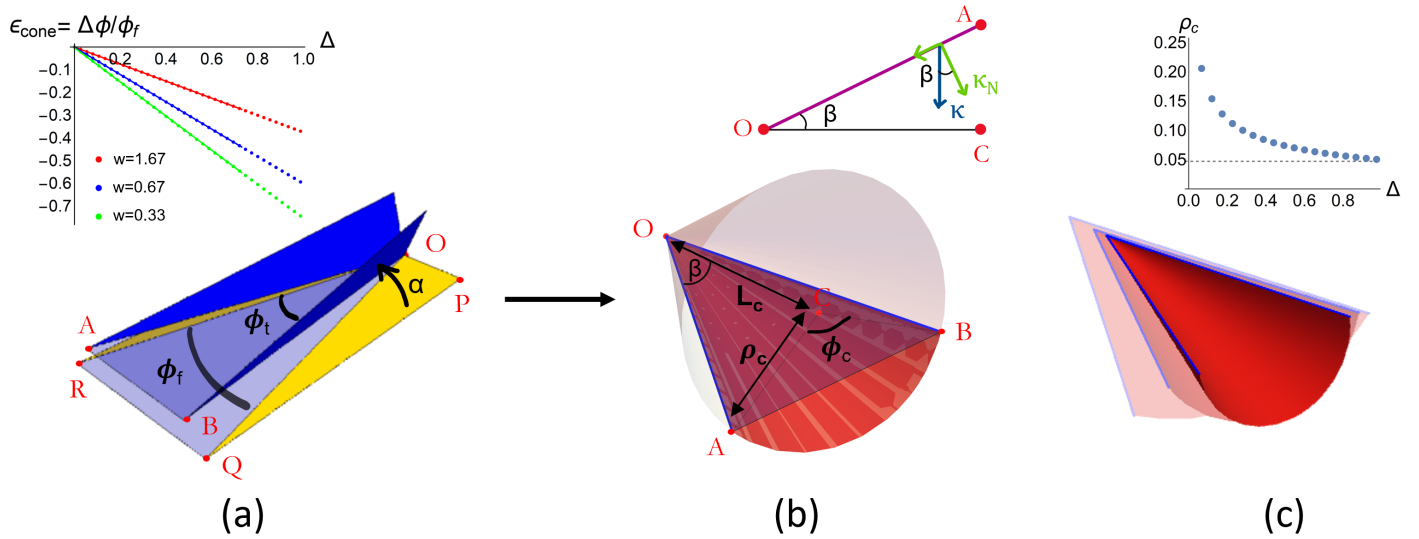
Fig. 7 Constructing a single cone (a) Two adjacent flat triangles (in yellow) subtending an angle ϕ_f tilt towards each other by angle α. The tilted triangles (in deep blue) subtend a smaller angle ϕ_t. Thus, the region between the triangles (shown approximately as a violet triangle) gets *squeezed* by an angle $\Delta\phi = \phi_t - \phi_f$. (inset) Evolution of the conical strain $\varepsilon_{\text{cone}} = (\Delta\phi)/\phi_f$ with Δ for three different widths w. Model measurements are plotted alongside the predicted lines of slope $= -1/(1+w)$ (see Eq. 13). (b) To fit within the contracted boundary defined by OA and OB, the region must bend into a circular cone of radius ρ_c, angular extent ϕ_c, axial length L_c and tilt angle β. The only ingredients needed for the construction are $\triangle AOB$ and the tilt angle $\alpha(\Delta)$. (inset) Cross-section of the cone (in magenta) through $\triangle OAC$, showing that the arc curvature κ and the normal curvature κ_N are related by $\kappa_N = \kappa\cos\beta$. (c) The evolution of the conical solution with Δ (here, $0.05 \le \Delta \le 0.6$). Greater opacity means larger Δ; the cones are translated with respect to each other for viewing clarity. (inset) As Δ increases, the radius of curvature ρ_c decreases, and for $\Delta \to 1$, attains an asymptotic value of $\rho_c \approx \frac{\pi w}{2m}$ (dotted line).
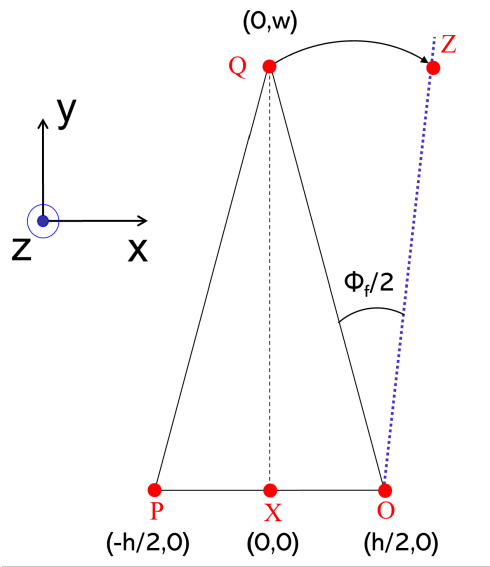

Fig. 8 Diagram supporting the calculation in Sec. 6.3. Triangle OPQ is the same as in Fig. 7a. Here, we give the points explicit coordinates (shown in black text). For more details, see main text.

midpoint of the edge QR, so that the bisector of the cone is the line OZ, shown as a dotted blue line in Fig. 8. The angle between OQ and the blue dotted line is then $\phi_f/2$.

This triangle is then tilted clockwise out-of-plane about $\overrightarrow{XQ}$ (parallel to the y-axis). Under this rotation, $P \to P'$ and $O \to O'$, while X and Q remain unchanged. In this tilted configuration, $\phi_t/2$ is given by the angle between the rotated vector $\overrightarrow{O'Q}$ and the

vertical blue plane defined by $\overrightarrow{OZ}$. In what follows, we use vector notation to denote both 3d and 2d vectors, precising their nature where necessary. The steps for determining ϕ_t are as follows:

1. Find the 3-vector $\overrightarrow{XO'} = \mathbb{R}_{-\alpha} \cdot \overrightarrow{XO}$, where $\mathbb{R}_\alpha$ is the standard 3x3 rotation matrix of angle α about the y-axis (positive α is considered anti-clockwise), and $\overrightarrow{XO} = (h/2, 0, 0)$.

2. Then $\overrightarrow{O'Q} = \overrightarrow{XQ} - \overrightarrow{XO'} = (-h/2\cos\alpha, w, h/2\sin\alpha)$.

3. We only need its orthogonal projection on to the x-y plane: the 2-vector $\overrightarrow{O'Q_\perp} = (-h/2\cos\alpha, w)$.

4. We need the vector angle between this and the vertical blue plane defined by $\overrightarrow{OZ}$. Here, $\overrightarrow{OZ} = \mathbb{R}_{-\phi_f/2} \cdot \overrightarrow{OQ}$, where $\overrightarrow{OQ} = (-h/2, w, 0)$.

Finally, we have $\phi_t/2 = \text{VectorAngle}[\overrightarrow{O'Q_\perp}, \overrightarrow{OZ}]$. Calculating this in a symbolic software like Mathematica, we get a complicated trigonometric expression that depends on three variables: α, ϕ_f, and the dimensionless triangle aspect ratio h/w.

To simplify this expression, we consider the regime of large m, which corresponds to both small h/w and small ϕ_f. Expanding to first order in h/w, and using the exact relation $\cos\alpha = 1 - \Delta$ to replace α by Δ, we get:

$$\phi_t = \phi_f - \frac{h}{w}\Delta + \mathcal{O}((h/w)^2) \qquad (11)$$

Thus, we get for the cone contraction factor:

$$\varepsilon_{\text{cone}} \equiv \frac{\phi_t - \phi_f}{\phi_f} \approx -\frac{h}{w\phi_f}\Delta. \qquad (12)$$

Substituting $h/w \approx \frac{\pi}{mw}$ and $\phi_f \approx \frac{\pi(1+w)}{mw}$ (valid for large m), we get:

$$\varepsilon_{\text{cone}} \approx -\frac{1}{1+w}\Delta. \qquad (13)$$

Eq. 13 predicts that, for large m, the slope of $\varepsilon_{\text{cone}}$ vs. Δ should be given by the ratio of inner to outer radius of the annulus. We plot this prediction as solid lines alongside the measurements in the inset of SI Fig. 7a. The two are fully consistent. While Eq. 13 for the slope has been shown only in the regime of narrow cones, in practice, we find it to be approximately valid even for wider cones. The qualitative conclusion here is that, for given Δ, wider annuli *effectively* feel less squeezed than narrower annuli in a cone-triangle deformation, independent of the number of triangles/cones.

6.4 Calculating bending energy for a cone

In this section, we continue with the variables introduced in Sec. 6.1. A right-circular cone is made up of a series of circles whose radii ρ increase linearly with distance (say, ζ) along the cone axis, measured from the cone tip. For a cone of axial length L_c (see SI Fig. 7a) and maximum radius ρ_c, we thus have: $\rho(\zeta) = \frac{\rho_c}{L_c}\zeta$. We can also write $\frac{\rho_c}{L_c} = \tan\beta$, where β is the cone's vertex angle.

Now, consider an infinitesimally wide circular band on the cone, of radius ρ, angular extent ϕ_c, and width $\frac{d\zeta}{\cos\beta}$. The band has bending energy $dU = \frac{B}{2} \times \kappa_N^2 \times (\phi_c\rho) \times \frac{d\zeta}{\cos\beta}$, where B is the bending modulus and κ_N is the local normal (i.e. out-of-plane) curvature. Given the geometry of the cone, we have $\kappa_N = \kappa\cos\beta$, where $\kappa = 1/\rho$ is the arc curvature of the circular band. Thus $dU = \frac{B}{2} \times (\cos\beta/\rho)^2 \times (\phi_c\rho) \times \frac{d\zeta}{\cos\beta}$. Simplifying and integrating over an entire conical sector gives:

$$U_{\text{bend}}^{\text{cone}} = \frac{B}{2}\phi_c\cos\beta\int_0^{L_c} d\zeta\,\frac{1}{\rho(\zeta)} \qquad (14)$$

$$= \frac{B}{2}\phi_c\frac{\cos\beta}{\tan\beta}\int_0^{L_c}\frac{d\zeta}{\zeta} \qquad (15)$$

The singularity as $\zeta \to 0$ means that the conical shape must be modified there. Thus we consider only the region beyond some L_{core}.

$$U_{\text{bend}}^{\text{cone}} = \frac{B}{2}\phi_c\frac{\cos\beta^2}{\sin\beta}\log(\frac{L_c}{L_{\text{core}}}), \qquad (16)$$

where $\beta = \tan^{-1}\frac{\rho_c}{L_c}$. For the majority of numerical samples discussed in this paper, where $m \gg \max\{1, 1/w\}$, it is sufficient to use small-angle approximations for β. Thus, setting $\cos\beta \approx 1$ and $\sin\beta \approx \beta$, Eq. (16) gets reduced to :

$$U_{\text{bend}}^{\text{cone}} \approx \frac{B}{2}\phi_c\frac{L_c}{\rho_c}\log(\frac{L_c}{L_{\text{core}}}), \qquad (17)$$

Here, ϕ_c, ρ_c and L_c are all functions of the contraction Δ. But ϕ_c and ρ_c are related through the constraint: $\phi_c\rho_c = L = \frac{\pi(1+w)}{m}$ (see Eq. 8), and $L_c \approx w$ (the width of the annulus), so $U_{\text{bend}}^{\text{cone}}$ can be reduced to a function of the single dynamic variable $\rho_c(\Delta)$. For the entire annulus, we need to multiply this by the number of cones $2m$. Thus, we get:

$$U_{\text{bend}}^{\text{cone}} \approx B\frac{\pi(1+w)w}{\rho_c^2(\Delta)}\log(\frac{w}{L_{\text{core}}}), \qquad (18)$$

More generally, for a cone extending between axial limits $L_{\min}$ and $L_{\max}$, we have:

$$U_{\text{bend}}^{\text{cone}}(\Delta) \approx B\frac{\pi(1+w)w}{\rho_c^2(\Delta)}\log(\frac{L_{\max}}{L_{\min}}), \qquad (19)$$

This is the expression given in the main text.

While Eqs. (18) and (19) seem independent of m, it is not so. Eq. (7) in the main text shows that $\rho_c \sim (1+w)/m \implies U_{\text{bend}}^{\text{theory}} \sim m^2$, as expected of a bending energy. We note that this $\rho_c \sim 1/m$ scaling could have been predicted in another way. In the limit of maximum possible contraction ($\Delta \to 1$), the point C approaches the xy-plane, and so the diameters of the $2m$ circles must approximately equal the reduced projected outer perimeter: $2\pi(1+w-\Delta) \to 2\pi w$. This gives us: $4m\rho_c \to 2\pi w \implies \rho_c \to \frac{\pi w}{2m}$ (the dotted line in the inset of SI Fig. 7c). Indeed, even if C is off the x-y plane (e.g. for smaller Δ), the diameters of the $2m$ circles must still equal the reduced perimeter $2\pi(1+w-\Delta)$ up to some factor. Thus, we have the scaling relation $\rho_c \sim 1/m$ as expected.

Finally, we note that the data presented in the paper represents the full expression 16, without any approximation.

6.5 Limits of the cone-triangle construction

To the best of our knowledge, the above conical construction works as long as the initial (flat) angle $\phi_f < \pi$, i.e. as long as the edges of two adjacent triangles define a triangle. The value of ϕ_f depends on the width w and the wavenumber m, and increases as m decreases. This defines a minimum wavenumber $m_{\min}^{\text{cone}}(w)$ below which a conical solution is invalid. For a sufficiently wide annulus, we find that $m_{\min}^{\text{cone}} = 2$, which is the minimum possible value for *any* wrinkled solution. However, for very narrow annuli, this value goes up. Thus, for $w = 0.2$, we find $m_{\min}^{\text{cone}} = 4$. Fig. 9 shows two such contrasting geometries. $m_{\min}^{\text{cone}}(w)$ defines a geometric limit beyond which we expect our cone-triangle model to fail. However, the main text shows that we already see significant deviations from our model for Abaqus solutions with wavenumber m significantly higher than $m_{\min}^{\text{cone}}(w)$.
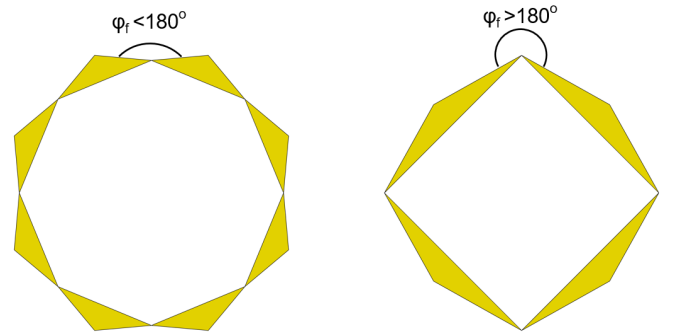

Fig. 9 Two different flat state geometries for $w = 0.2$. (Left) For $m = 4$, the flat angle $\phi_f < \pi$, which allows the conical construction described in Sec. 6.5. (Right) For $m = 2$, the flat angle $\phi_f > \pi$, which means that our conical construction is not valid here.

6.6 Comparison with separable, sinusoidal wrinkling

The cone-triangle shape described in the main text sharply reduces the elastic strain and energy relative to conventional wrinkling with height profile $h^c(r, \theta)$ *e.g.* of the form[17]

$$h^c(r, \theta) = f(r)\cos(m\theta) \qquad (20)$$

as we now illustrate.

In the far-from-threshold regime, this h^c profile must relax the azimuthal strain $\varepsilon_{\theta\theta}$ arising from the inward displacement $u_r = -\Delta$. In general this azimuthal strain has the form[2]:

$$\varepsilon_{\theta\theta} = \frac{u_r}{r} + \frac{1}{r}\partial_\theta u_\theta + \frac{1}{2r^2}(\partial_\theta h^c)^2 \qquad (21)$$

For purposes of comparison we may evaluate this ε at a zero of $h^c(r,\theta)$ *e.g.* $m\theta = \pi/2$. There by symmetry the azimuthal displacement $u_\theta = 0$ and $\partial_\theta u_\theta = 0$. Thus the second term in Eq. 21 vanishes. In the last term $\partial_\theta h^c = \pm m f(r)$. We use this expression to estimate $\varepsilon_{\theta\theta}$. Choosing $h^c(r,\theta)$ to make $\varepsilon_{\theta\theta}$ vanish implies

$$\Delta \simeq \frac{1}{2r}m^2 f(r)^2 \qquad (22)$$

So that $f(r) \simeq \frac{1}{m}\sqrt{2r\Delta}$

This non-constant $f(r)$ entails a radial strain ε_{rr} given by[2]

$$\varepsilon_{rr} = \partial_r u_r + \frac{1}{2}(\partial_r h)^2 \qquad (23)$$

Here u_r is constant as noted above and $\partial_r h \simeq \partial_r f(r) \simeq \frac{1}{m}\frac{1}{2}\sqrt{2\Delta/r}$, giving an estimated conventional wrinkle strain ε_{rr}^c of

$$\varepsilon_{rr}^c \simeq \frac{1}{4}m^{-2}(\Delta/r) \qquad (24)$$

This radial strain of conventional wrinkling is to be compared to the bending strain ε^B in the cone-triangle model. This strain arises from the bending stress $\sigma_{\theta\theta}^B$ [17]

$$|\sigma_{\theta\theta}^B| \simeq 2B(m/2\pi r)^2, \qquad (25)$$

where bending modulus B is related to the thickness t, the Poisson ratio ν and the bulk Young's modulus E by[39] Sec.12

$$B = Et\frac{t^2}{12(1-\nu^2)}. \qquad (26)$$

Using $\varepsilon = (Et)\sigma$, then Eq. 25 yields

$$\varepsilon_{\theta\theta}^B \simeq 2\frac{t^2}{12(1-\nu^2)}(m/2\pi r)^2 \qquad (27)$$

For the annuli simulated above the conventional wrinkles have much greater elastic strain than the bending strain we report: their ratio is given by

$$\frac{\varepsilon^c}{\varepsilon^B} \simeq m^{-4}(r\Delta/t^2)\left(6(1-\nu^2)\pi^2\right) \qquad (28)$$

Evidently for fixed m the ratio diverges as $t \to 0$. For the specific annulus used for Fig 5 with $r = 1$, $\Delta = 0.2$, $\varepsilon^c/\varepsilon^B \simeq 50$. By these estimates the sinusoidal wrinkling carries substantially larger strain and thence elastic energy relative to the isometric wrinkling we

report.

6.7 Departures from conical shape

Here we gauge the impact of the stretched zigzag vertices on the total energy by examining how the elastic energy varies with distance $r - 1$ from the inner rim. Fig. 10a shows this energy for the right-most data points of Fig. 5. The red simulation point (lower curve) in Fig. 5 is found by summing the energies in each azimuthal ring of finite elements over the range of r indicated by the hashed region. The simulated ring energies for selected r are shown as black rectangles.

The corresponding cone-triangle energy, *i.e.* the right-most point on the (yellow) middle curve in Fig. 5, is found using the cone ring energy plotted as a solid curve, using Eq. 5. This equation implies a ring energy varying as $1/(r-1)$. Since the yellow point is found by matching the simulated curvature at the outer boundary, the cone model gives a ring energy that matches the simulated ring energy there, as Fig. 10a shows.

By comparing the simulated ring energies with the cone model, we can gain insight into the difference in energies seen in Fig. 5. The inner simulation point shows the expected large discrepancy with the model, which unrealistically diverges at the inner boundary. The middle simulation point is at the inner boundary of the region treated in Fig. 5. This ring energy is 40 percent smaller than the cone model prediction. This difference is consistent with the 15 percent differences between the energies of Fig. 5. Any cone that would cure this discrepancy would have to extrapolate to a vertex beyond the inner boundary.

The azimuthal strain profile shown in Fig. 10b also shows departures from the model. The plot shows the azimuthal dependence of the azimuthal strain $\varepsilon_{\theta\theta}$ for a radial position r equidistant between the inner and outer boundaries.. The plotted strain is maximal at peaks and troughs of the wrinkles. Though the averaged strains,are consistent with bending strains, as discussed in Sec. 3.1, there are strong oscillations adjacent to these peaks and troughs with a period of two finite elements. This suggests that our simulations have limited reliability for predicting these weak strains near the peaks or troughs. Away from the peaks and troughs the strains vary smoothly. Of special interest is the point where the model cone and its adjacent triangle would meet. These points, marked by dashed lines show no sign of discontinuity.

These detailed features of Fig. 10 show shortcomings of the cone-triangle model. However they underscore the relevance of this model for understanding this form of buckling.

6.8 Finite-element method (FEM) simulation details

For our simulations, we used the commercial finite-element software Abaqus 2018 (Simulia, Dassault-Systèmes, Providence, RI). This section describes the different steps for generating a typical simulation of our inner Lamé system, in the order typical of a finite-element software.

The assembly consisted of only a single annulus, with inner radius fixed and taken to be unity, and with varying width w and thickness t in order to test our system over a wide
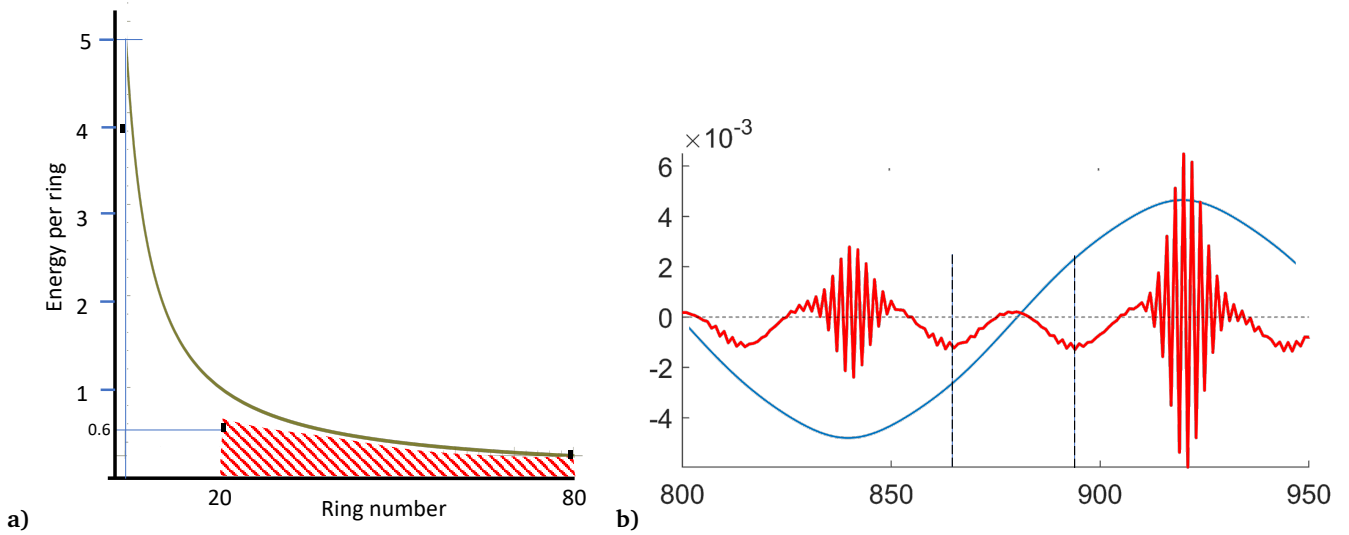
Fig. 10 a) Energy distributions for the annulus of Fig. 5. Horizontal axis is radial distance from inner rim measured in finite element widths. Vertical axis is ring energy described in the text. Hashed region shows the region treated in Fig. 5. Its area represents the simulated energy with largest Δ on the lower curve of Fig. 5. Black marks show simulated ring energies at three selected radii. Solid curve shows the ring energy profile calculated from cone-triangle model used for the middle curve in Fig. 5. b) Simulated azimuthal strain $\varepsilon_{\theta\theta}$ (in red) as a function of azimuthal finite-element coordinate θ, for a material circle located at the middle of an annulus with ($w = 0.33$, $t = 1.33 \times 10^{-3}$, $m = 10$, $\Delta = 0.27$). Light curve in blue shows height profile. Region spanning one trough and peak are shown. Variability of other troughs and peaks is similar. Vertical black lines indicate the location of two consecutive cone-triangle boundaries.

range of system parameters. For width, we used values $w = 0.20, 0.33, 0.67, 1.0, 1.67$ (a factor of almost 10, ranging from very narrow to moderately wide), and for thickness, we used values $t = 2.67 \times 10^{-3}, 1.33 \times 10^{-3}, 6.67 \times 10^{-4}, 2.67 \times 10^{-4}, 1.33 \times 10^{-4}$ (a factor of 20, ranging from moderately thick to very thin). While these thickness values vary over a decade, the values still fall well within the thin sheet limit. The annular part was made of 2d shell quad (S4R) elements[40]. This choice was made mainly to optimise speed, since we used a fine enough mesh to ensure that doubling the linear mesh size change the energy by a negligible amount ($\lesssim 1 - 2\%$). For comparison, the coarsest mesh we used was for the $w = 1.67$ annulus, with 60 elements across the radius and 1400 elements across a circle, giving a maximum linear size for an element ≈ 0.01. For consistency checks however, we also ran some simulations with annuli made of 3d volume cubic (C3D8R) elements[40], which gave the same morphology (with the same wavenumber), but which much longer running times.

When discussing the material properties, for concreteness, we will use SI units (and thus take the inner radius to be 1 m). For the material properties, we mostly used a standard neo-Hookean hyperelastic model[40] with coefficients $C_{10} = 1.5375 \times 10^5$ Pa, $D_1 = 3.2520 \times 10^{-7}$ Pa^{-1}. These coefficients are related to the more well-known linear elasticity moduli by the relations: $C_{10} = G/2$ (where G is the shear modulus), and $D_1 = 2/K$ (where K is the material bulk modulus). The corresponding Poisson ratio is given by $\nu = \frac{3/(C_{10}D_1)-2}{6/(C_{10}D_1)+2} = 0.475$. The Young's modulus can be obtained from either of the relations: $E = 2G(1+\nu)$, or $E = 3K(1-2\nu)$; we obtain $E = 907,377$ Pa ≈ 0.9 MPa (corresponding to a rubber-like material). As a test, we also performed several simulations with a linear material model with these values of E and ν.

The elastic modulus can be used, along with the material density ρ and the average linear mesh size l_e, to determine the aver-

age integration time scale (i.e. the 'stable time increment') in the simulation, as follows. The elastic bulk modulus K and the density ρ determine the speed of sound in the material, $c_s = \sqrt{K/\rho}$ [††]. The stable time increment in the simulation is on the scale of the time required for elastic information to traverse an average mesh element: $\Delta t \sim l_e/c_s$. For our values of $K \sim 10^5$ Pa, $\rho = 10^3$ Kg/m^3 and $l_e \sim 10^{-2}$ m, we get $\Delta t \sim 10^{-3}$ s. This in turn determines the dimensionless number of iterations n_{iter} performed by the solver in a simulation running over time period T: $n_{\text{iter}} = T/\Delta t$. Below, we discuss the typical values of T used in our simulations, and how increasing T allows us to reach a quasi-static limit in dynamic integration methods (i.e. where kinetic energy is present but negligible compare to elastic energy).

For the radial displacement loading at the inner boundary, we applied velocity and displacement boundary conditions (BCs) interchangeably. Typically, we applied velocity BCs with a linear amplitude profile, and displacement BCs with a smooth-step profile[40], in order to assure a smooth (i.e. zero velocity) pull at the beginning. These were applied so that the maximum displacement amplitude $\Delta_{\text{max}} = 0.267$ is attained within a time period T (defined in the same units as the Δt given above). The value of T was chosen to be large enough to ensure small kinetic energy and give a T-independent configuration, as defined below. Typically, we used $T = 20$ for the thicker sheets, and $T = 80$ for the thinnest sheets.

For the simulation protocol, we employed both 'dynamic explicit' and 'dynamic implicit'[40] integration schemes in the quasi-

---

[††] Alternately, one can use the Young's modulus E instead of the bulk modulus K in the definition of c_s. But this does not qualitatively alter our argument above.

static limit (as compared to a fully 'static' energy minimisation scheme). The word 'dynamic' refers to the presence of inertia, while 'explicit' and 'implicit' refer to the solution scheme. 'Explicit' means explicit time-integration of Newton's second law, while 'implicit' refers to implicit integration (viz. through iterative root-finding) of Newton's law, using a modified Newton-Raphson method. The mixture of these two methods was done partly as a consistency check, partly for convenience, and partly by necessity. While the implicit method in the quasi-static limit was faster for most jobs, the explicit solver was indispensable for the thinnest samples, where the static solver ran into convergence problems. Ensuring the quasi-static limit is also easier for 'dynamic implicit' than for 'dynamic explicit'. In dynamic implicit, the quasi-static option is in-built, but for dynamic explicit, it has to be ensured manually by applying the loading slowly enough so that further slowing has no effect on the final shape and energy.

For this, we need to look at the available energy modes. The energy balance equation in Abaqus[40] is given by (ignoring possible terms coming from viscosity, friction, heat, contact and constraint penalties, etc.), is:

$$E_I + E_{KE} - E_W = 0 \qquad (29)$$

where E_I is the internal energy, E_{KE} is the kinetic energy, and E_W is the work done by externally applied loads. For us, the internal energy is just the elastic energy (by design, there are no other energy modes). Thus, for quasi-static loading, one generally requires the kinetic energy (E_{KE}) to be $< 10\%$ of the elastic energy (E_I). In practice, we kept the ratio to $\lesssim 5\%$. Since the elastic energy is thickness-dependent (always increasing with increasing thickness), thinner sheets required slower applications of the loading. E.g., for the thinnest samples ($t = 1.33 \times 10^{-4}$), this involved applying the contraction Δ over a time period $T = 80 - 120$, viz. using $n_{\text{iter}} \sim 10^5$ solver iterations. As a result, the slowest simulations, for the thinnest and widest sheets, lasted ≈ 150 core-hours; the average simulation however, lasted between ≈ 30 core-hours. For reference, the validation case (described blow) of fold-

ing a flat sheet into a cylinder, albeit with a much coarser mesh, was accomplished using ≈ 0.2 core-hours.

For data extraction, we used field output for the displacement variables, and history output for the energy[40]. For the elastic energy, we used the "ALLIE" (internal energy) variable[40], equivalent to the E_I variable in Eq. 29. Since the simulations are done using a dynamic time-integration scheme with inertia, there is an inherent noise in the energy values arising from imprecision in finding the exact energy minimum (viz. due to inertial oscillations). We cannot estimate this noise precisely, but a rule-of-thumb estimate is $\lesssim 5\%$, i.e. of the same order of magnitude as the ratio E_{KE}/E_I. However, in reality, it might well be less. Significantly, this noise cannot account for the discrepancy between energy measurements and model predictions in Fig. of the main text. Finally, post-processing was done using Abaqus2Matlab[37].

6.9 Testing the numerics for known cases

We used the above procedures (albeit with a static energy minimisation scheme) to calculate an analytically solvable case, to verify that the shape and energy agreed with the known results. The example was a rectangular sheet of width $w = 1$, length $L = 2\pi$, and thickness $t = 1 \times 10^{-3}$, in which we prescribed boundary conditions on position and orientation of the short edges to make them curve up and in, to form a circular cylinder of unit radius.

We verified the circularity of the cross-section by projecting onto the plane and measuring the distance from the centre. We found that no point differed in its axial distance by more than .001%. The measured elastic energy differed only slightly from the analytic result, $U_{\text{bend}}^{\text{cylinder}} = B\pi \approx 3.07 \times 10^{-4}$ Joule, where $B = Et^3/12(1 - v^2)$ is the bending modulus, obtained using the thickness t, Young modulus E and Poisson ratio v quoted above. The simulation gave an energy $\approx .01\%$ larger than this. A discrepancy of this sign is expected because the analytic form neglects the small strain energy owing to the nonzero thickness of the sheet simulated.

————————————————————